Supporting Information for "A Kalman Filter Time Series Analysis method for InSAR"

M. Dalaison[1], R. Jolivet[1,2]

[1]École Normale Supérieure, PSL Université, CNRS U.M.R. 8538, Laboratoire de Géologie, Paris, France

[2]Institut Universitaire de France, 1 rue Descartes, 75005 Paris, France

Introduction

The following additional Figures (S1 to S14) provide a graphical appreciation of the effect of parametrization on the behavior of the Kalman filter. Hence, most Figures are variants of Figures in the main text. Figures S1 to S9 are the results of the Kalman filter applied to the synthetic case (Section 3.1), whereas Figures S10 to S14 refer to the application on ENVISAT data over Mt Etna. The effect of 'wrong' parametrization is highlighted by deliberately imposing unrealistic values with respect to recommendations given in Section 3.1.3 and 4.1. We chose to detail the example on Mt Etna rather than on the Chaman fault as it forms a finite length dataset (while Sentinel data are continuously acquired) and it includes fewer pixels.

Corresponding author: M. Dalaison, Laboratoire de Géologie, École Normale Supérieure, 24 rue Lhomond, 75005 Paris, France. (dalaison@geologie.ens.fr)

Contents of this file

1. Figures **S1**.

Synthetic case covariance.

2. Figures **S2** and **S3**.

Effect of chosen parametric description of deformation on synthetic cases.

3. Figures **S4** to **S7**.

Effect of 'wrong' misclosure and mismodeling error on synthetic cases.

4. Figures **S8** and **S9**.

Impact of *a priori* error on synthetic cases.

5. Figures **S10**.

Number of available data points per pixel for the example of Mt Etna.

6. Figures **S11**.

Final parameters of the deformation model for the example on Mt Etna.

7. Figures **S12** and **S13**.

Effect of *a priori* and mismodeling errors for the example of Mt Etna.

8. Figures **S14**.

Instance of covariance matrices for the example of Mt Etna.

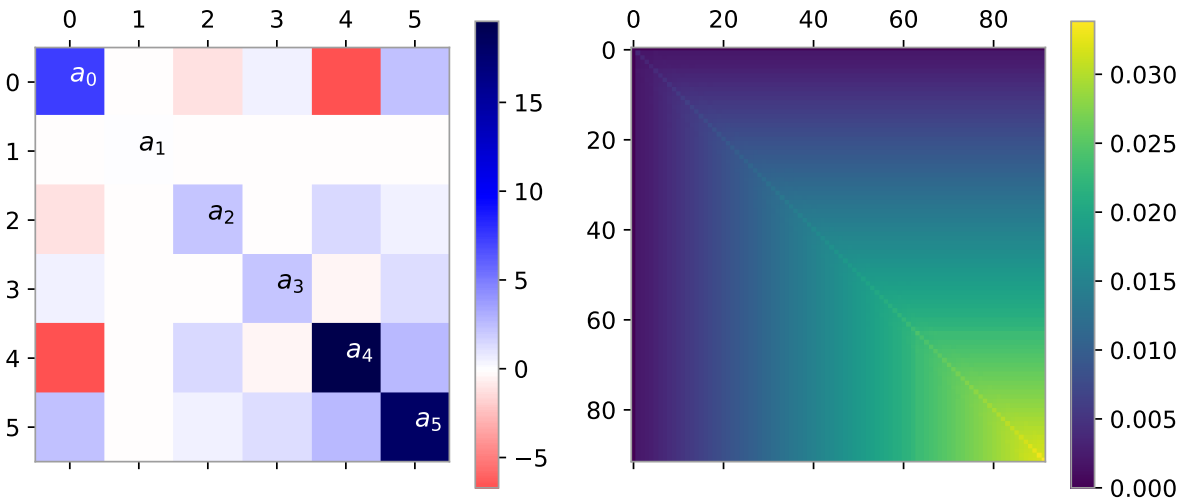

Figure S1. Graphical representation of the final Covariance matrix ($\mathbf{P}_{91}$) in the reference synthetic test (Section 3.1.2) for the same selected pixel than in Figure 3 and 5. Elements characterizing the variance-covariance of model parameters, a_n, (*left*) are represented separately from the variance-covariance of phase estimates, ϕ_k, (*right*). A striking feature on the *left* subplot, is how well the velocity a_1 is constrained with this optimally parametrized inversion. For other parameters, inter-dependency is strong, especially with the initial offset a_0. This is why we recommend to store out of the state vector parameters that have already converged (i.e. those for which new data is not informative). Notice the very small uncertainty and significant temporal correlation of phase estimates.

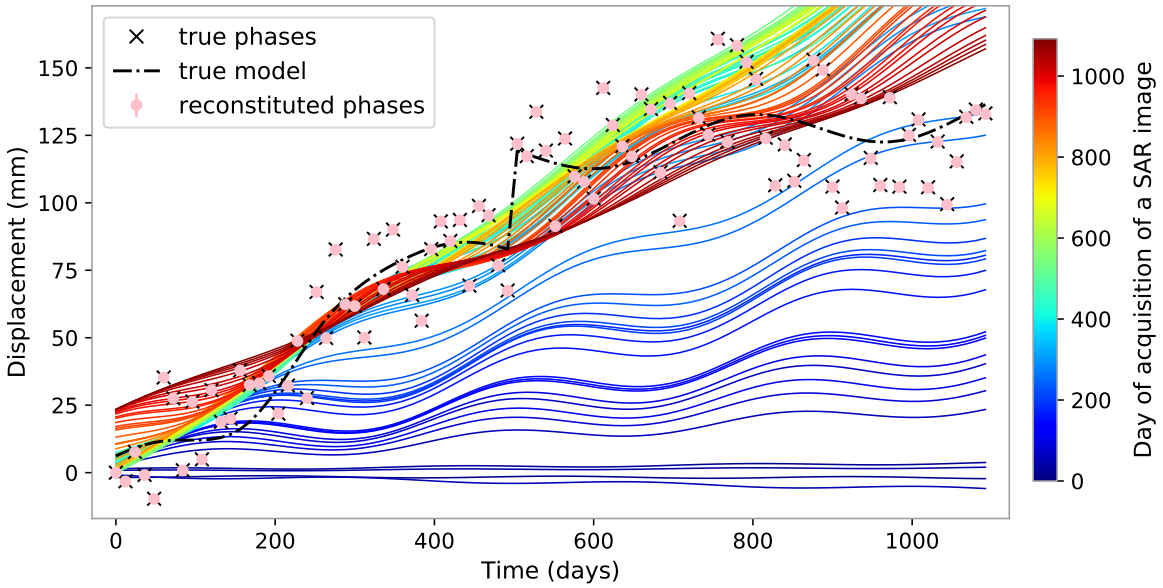

Figure S2. Same as Figure 3B for a parametrized model with missing step and spline components (i.e. a_4 and a_5 are excluded from the inverse problem). We can see that phase values are well retrieved even though model parameters are wrong with respect to the true value. Providing the same functional form is used, the match with least-squares solution is still true. Note that the correct retrieval of phases in the case of a 'wrong' model is possible providing the network of interferograms connects all dates to the initial and reference date.

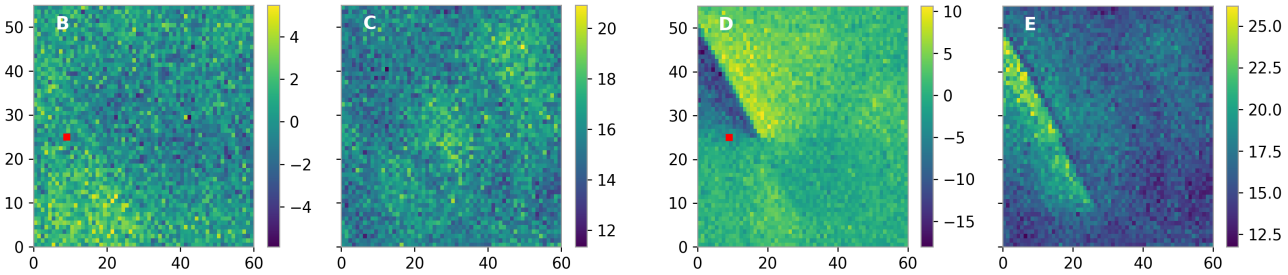

Figure S3. Median (B,D) and standard deviation (C,E) per pixel of the time series of mean innovation in the case of optimal parametrization (presented in Section 3.1.2) (B,C) and in the case of missing step and spline components in the description of deformation (D,E) (like in Figure S2). In real cases, the statistical **distribution of innovation** per pixel allows to clearly identify areas with 'wrong' model description, here those next to the simulated active fault. In this region, innovation is not normally distributed and the center of the distribution it not zero, which literally means that the forecast based on the parametrized model does not appropriately describe the phase evolution. In such case the model should be updated, and this can be done in between assimilation steps.

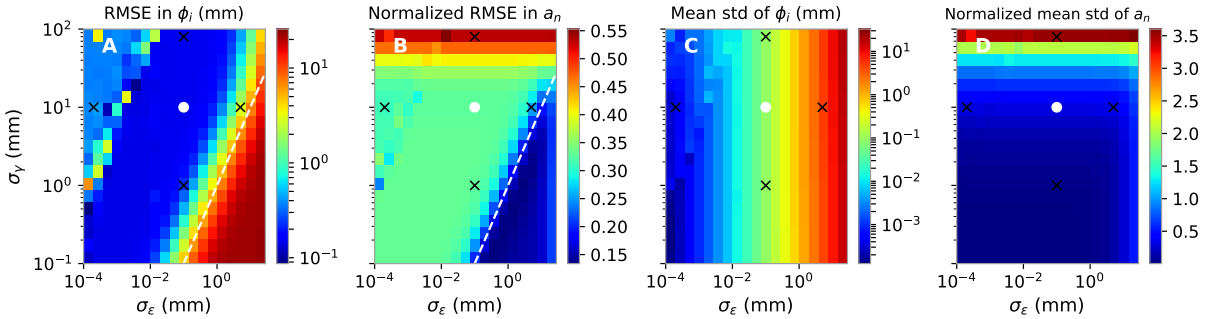

Figure S4. Same as Figure 6 with four additional crosses locating the (σ_γ, σ_ϵ) configuration of the cases presented in the 3 subsequent Supplementary Figures (S5-S7). Those examples are representative of the overall effect of reducing or increasing σ_γ or σ_ϵ.

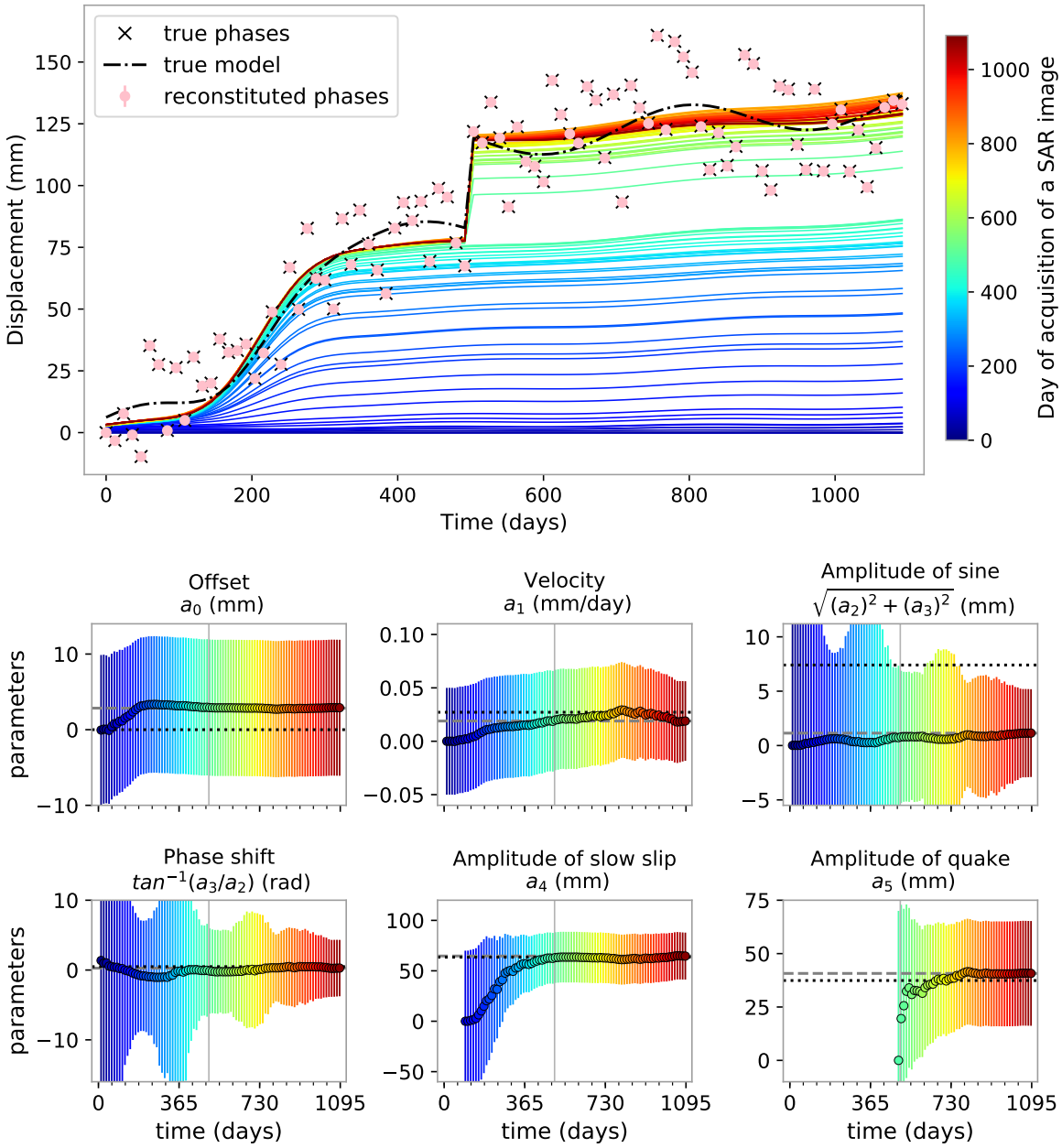

Figure S5. Same as Figure 3B and 5 for a large *a priori* standard deviation of the mismodeling error (σ_γ of 80 mm). This implies that we have little trust in the ability of the functional model to describe the phase evolution. Thus, model parameter uncertainties are very large. and more assimilation steps (and thus data over time) are needed for convergence of the functional description. Consequently, small seasonal oscillations are hardly adjusted for and the state vector remains close to its a priori value, $\mathbf{m}_0$, until enough data is assimilated.

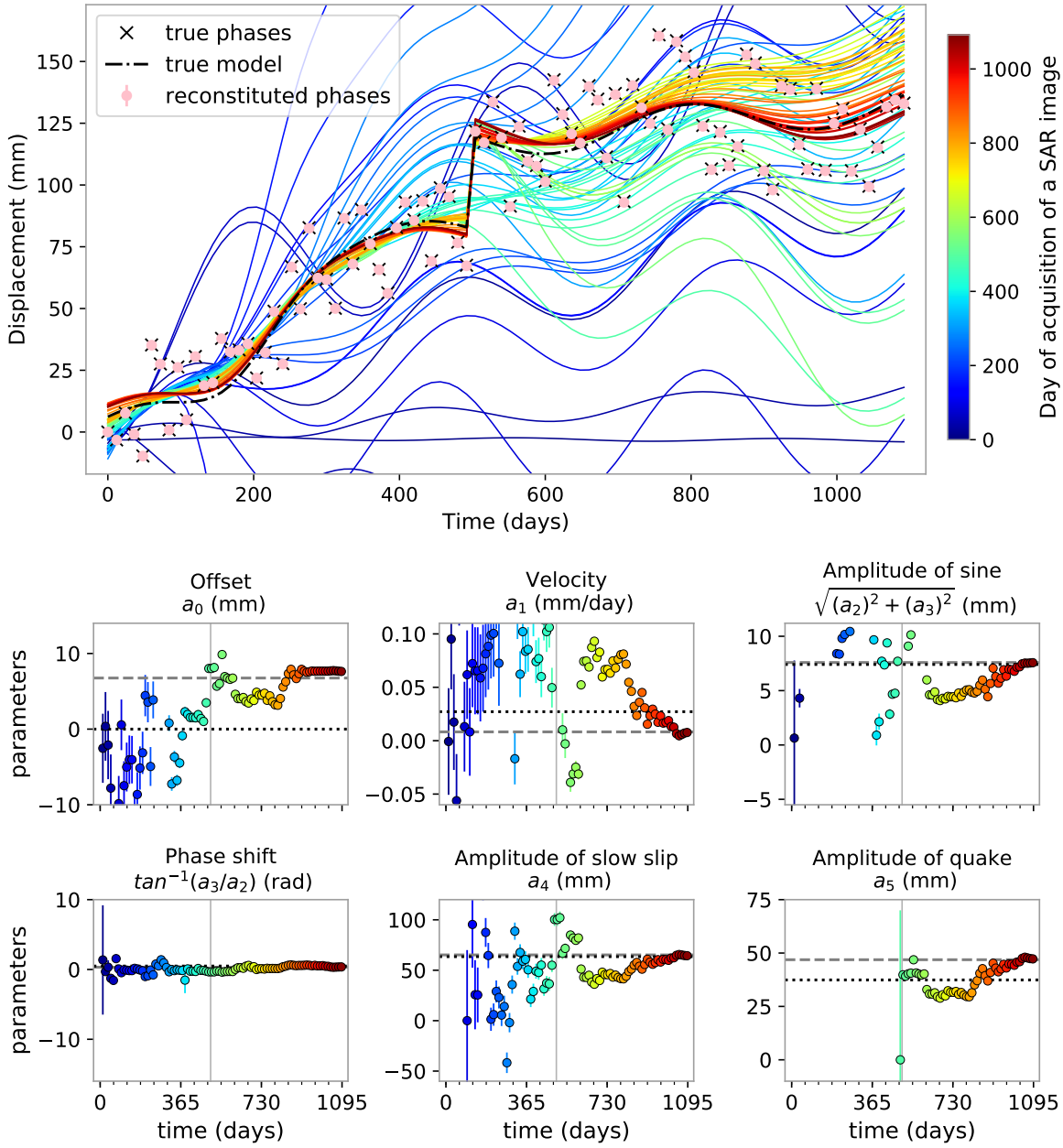

Figure S6. Same as Figure 3B and 5 for a low *a priori* standard deviation of the mismodeling error (σ_γ of 1 mm). This implies that we trust too much the ability of the functional model to describe the phase evolution. Thus, model parameter uncertainties drop quickly and the model is very sensitive to new data and tries to adjust at each new assimilation step. This is particularly marked when little data has been assimilated. The final estimation is not too biased but parameter uncertainties σ_{a_n} are clearly underestimated.

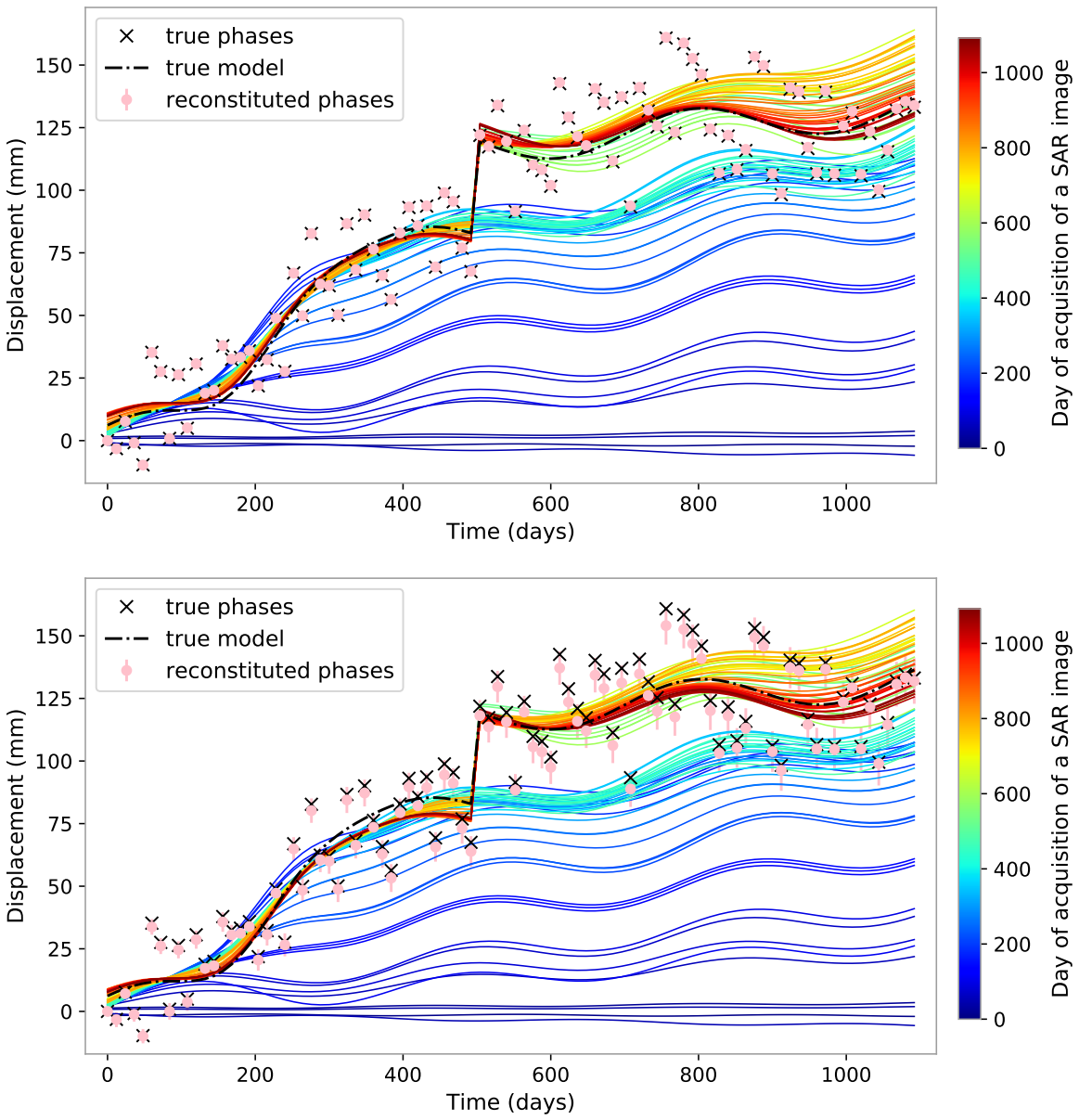

Figure S7. Same as Figure 3B for a very low (top) and high (bottom) *a priori* standard deviation of the misclosure error (σ_ϵ of 2×10^{-4} mm and 5 mm). Lowering σ_ϵ induces a subtle shift in phase estimate with respect to true value. This bias increases over time. On the other hand, increasing σ_ϵ lowers the confidence in the phase estimate. However, we have to underestimate σ_ϵ by 3 orders of magnitudes, or multiply the value by 50 (and, thus, get close to σ_γ) to notice a change in the graphical representation of the time series, which is consistent with the small sensitivity to this parameter.

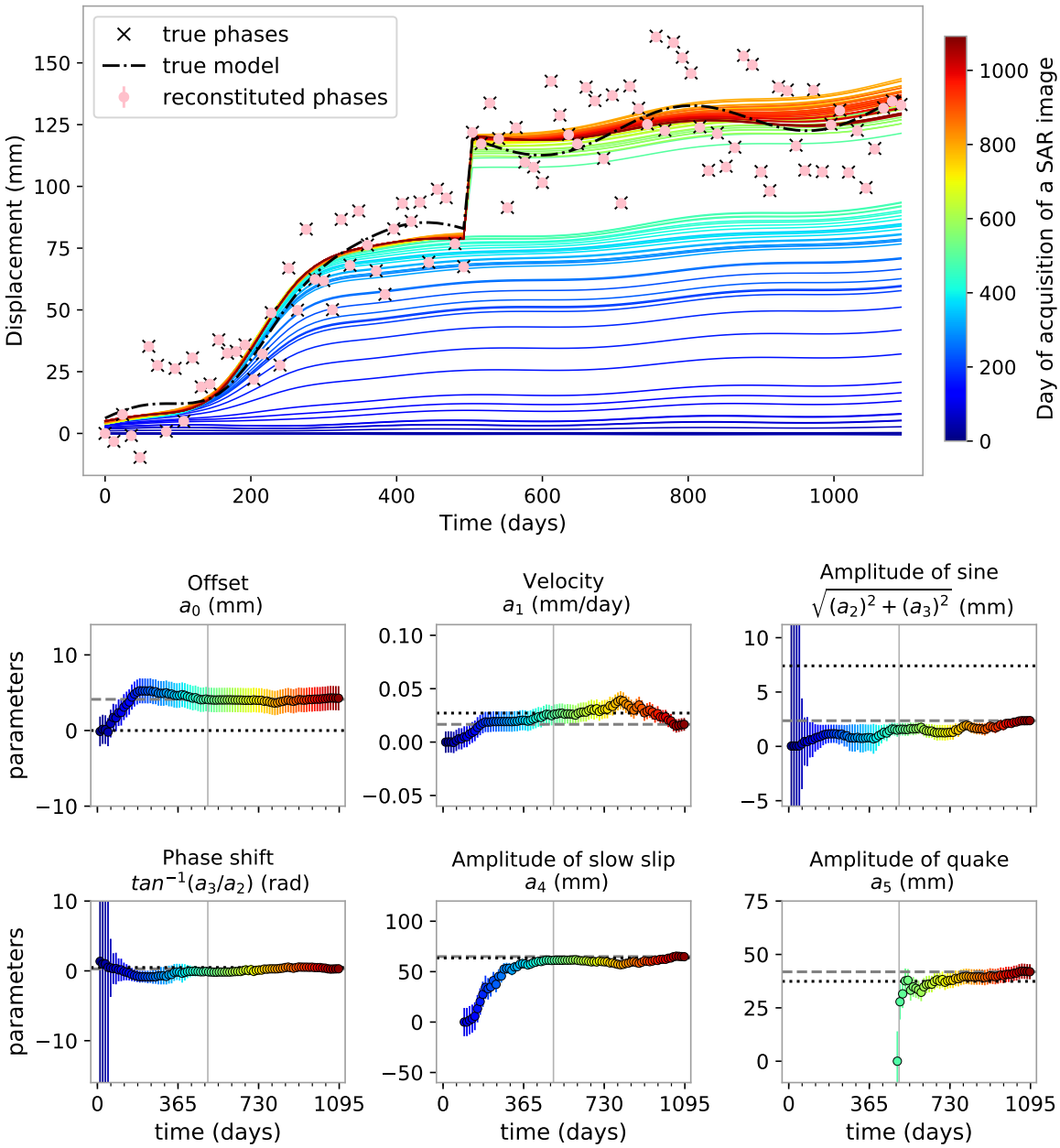

Figure S8. Same as Figure 3B and 5 for a very low *a priori* error on model parameters (all reference standard deviation σ_{a_n}, $0 \leq n < L$ in Section 3.1.2 have been divided by 5). As a consequence, there is great confidence in the initial null model and smoother solution is found. The role of σ_{a_n} as a regulation term is clearly outlined.

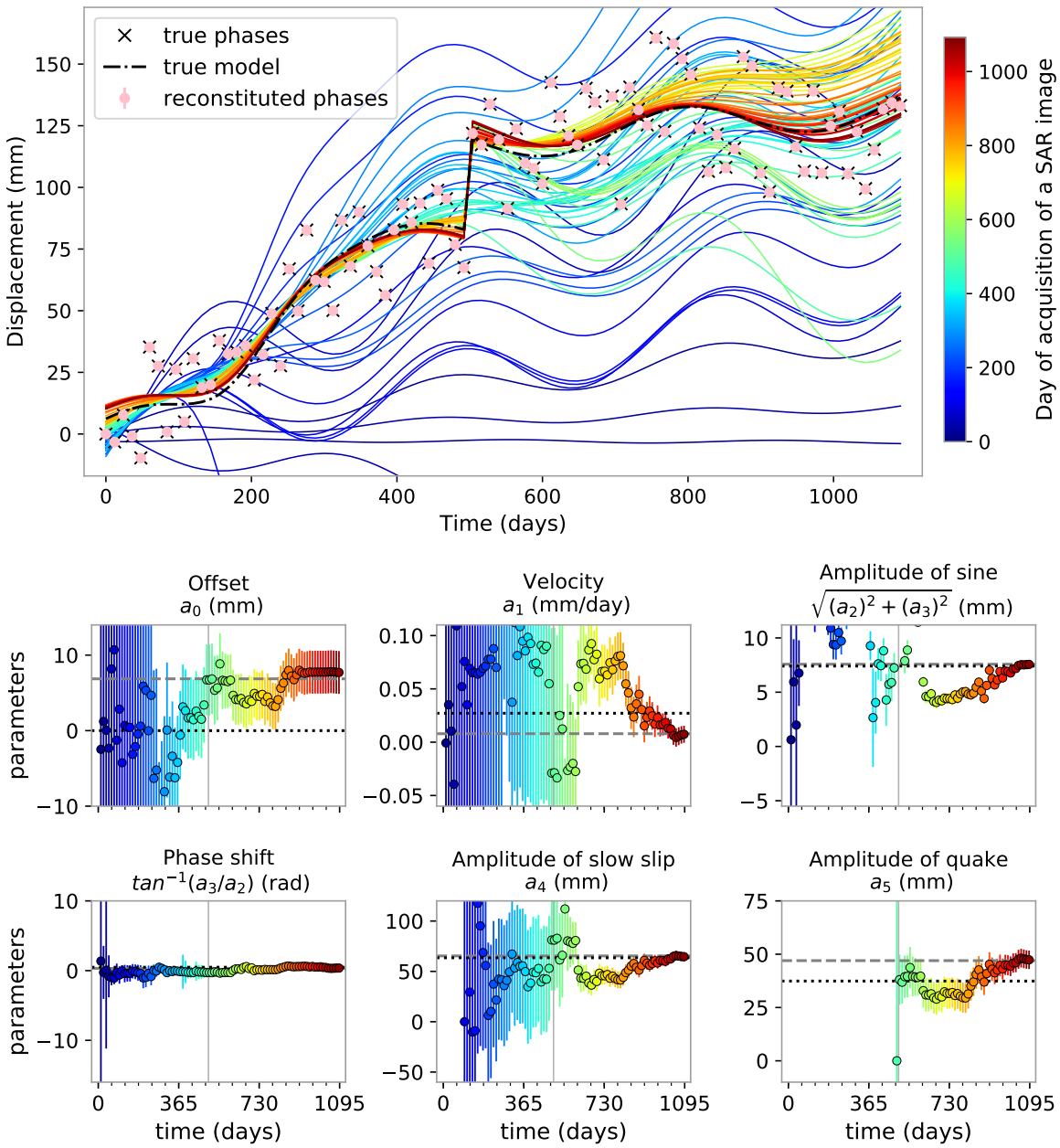

Figure S9. Same as Figure 3B and 5 for a very high *a priori* error on model parameters (all reference standard deviation σ_{a_n}, $0 \leq n < L$ in Section 3.1.2 have been multiplied by 5). As a consequence, the model parameters computed in the first assimilation steps is a lot more uncertain and is very sensitive to the new data assimilated. From Figures S6 and S7, it seems that the diagonal of $\mathbf{P}_0$ has the inverse effect than σ_γ on model parameter value (Figures S3, S4). However, the effect on parameters uncertainty differs (already outlined by Figure S0). Notice that the model progressively recovers, as data is assimilated, from 'bad' *a priori*.

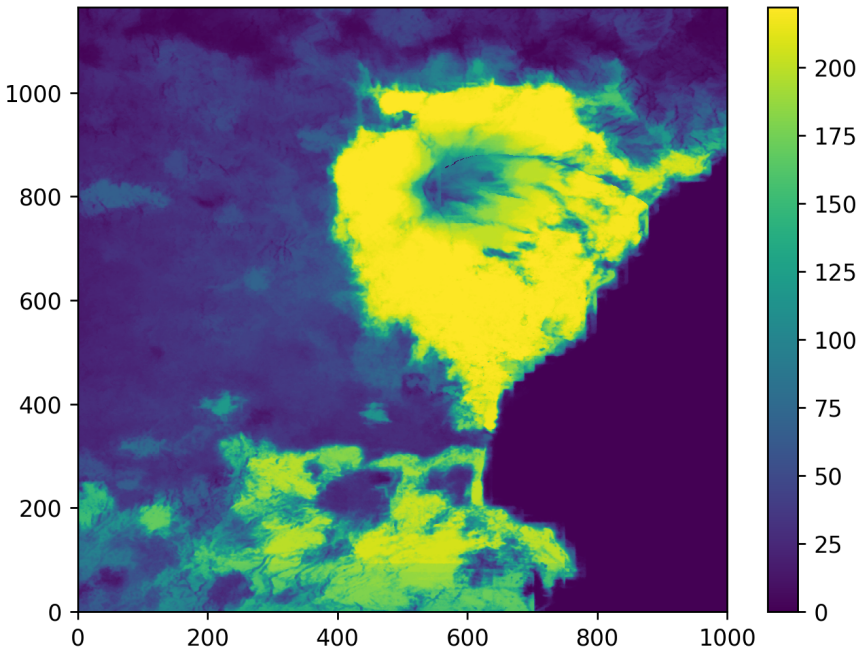

Figure S10. Number of interferograms available per pixel, which directly affects the phases (and parameters) variances (Figure 7B and S11).

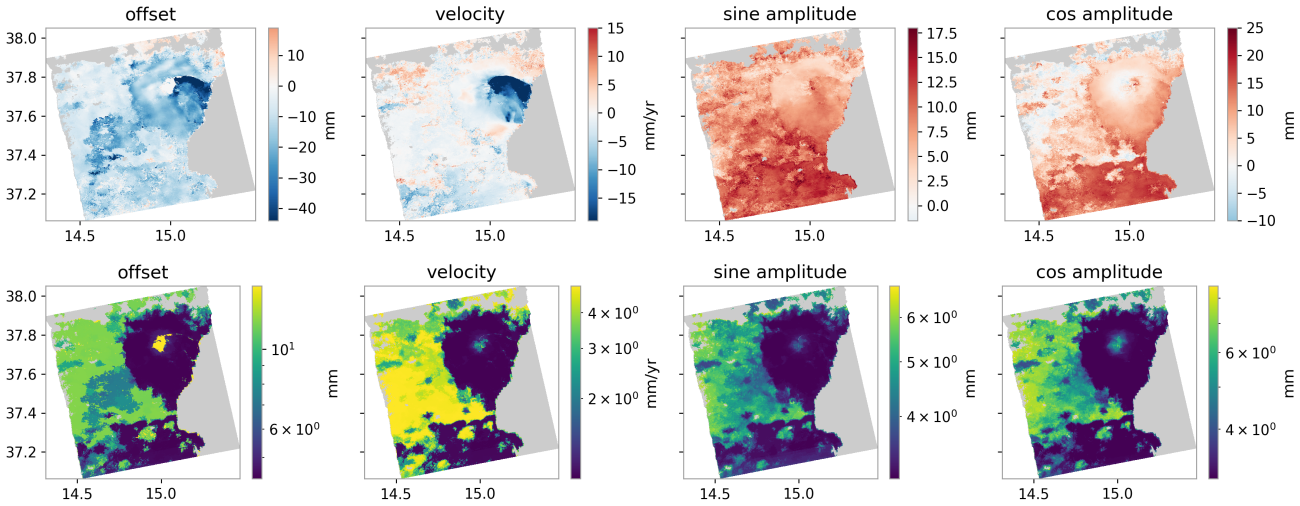

Figure S11. Model parameters, a_n, reconstructed for Mt Etna (top) and their standard deviation (bottom).

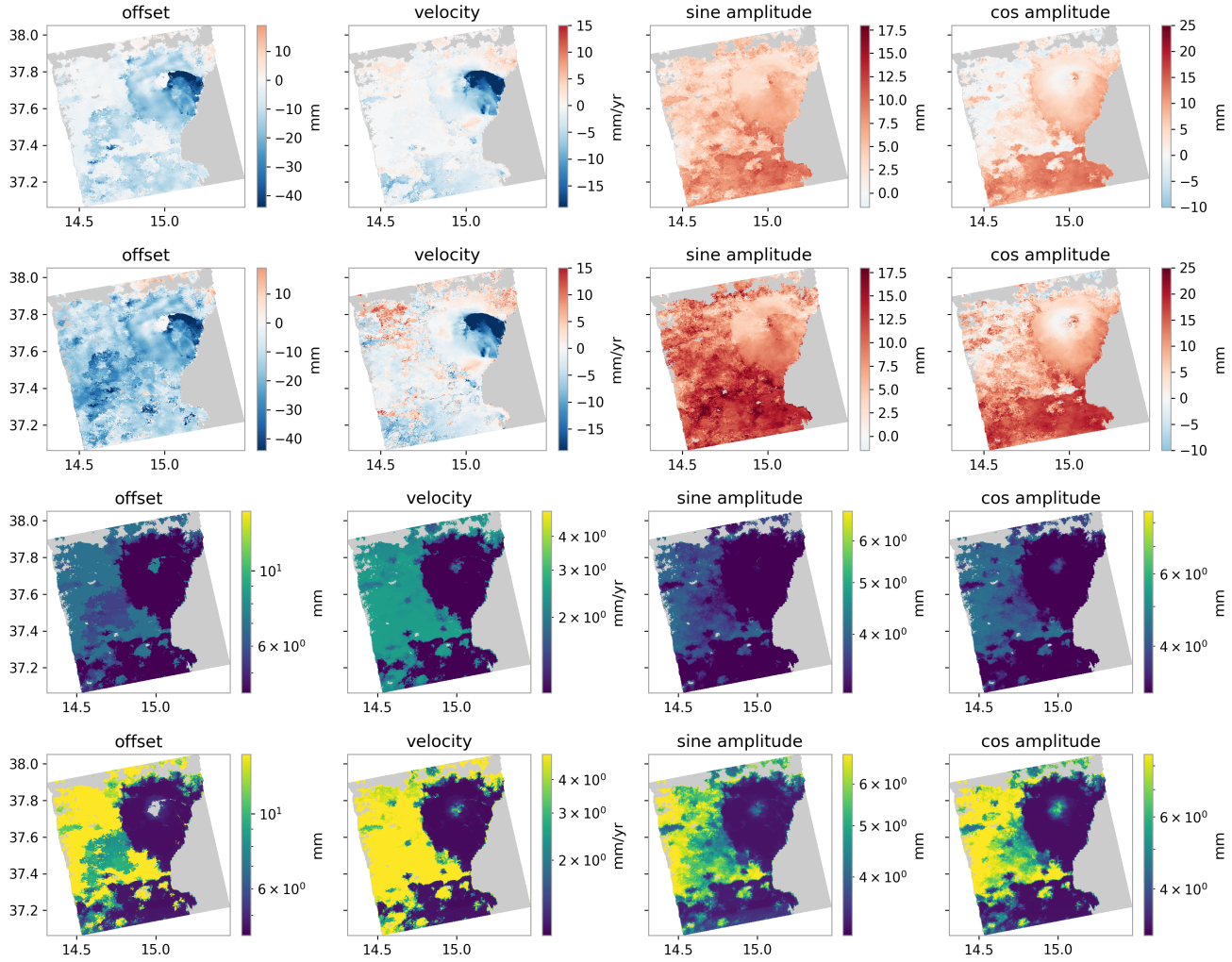

Figure S12. Same as Figure S11 for a Kalman filter for which $\mathbf{P}_0$ was changed. The standard deviation of *a priori* model parameters was either divided by 2 or multiplied by 2 with respect to reference case. Colorbars are bounded using the reference case in Figure S11 for easy comparison. Row by row from top to bottom: parameters for low $\mathbf{P}_0$, parameters for high $\mathbf{P}_0$, standard deviations associated with each parameter for low $\mathbf{P}_0$ and, below, for high $\mathbf{P}_0$. Notice the persistence of the dominant patterns on the volcanic edifice. Most of the differences concentrate in the plains surrounding the volcano with fewer data, hence a greater influence of the forecast.

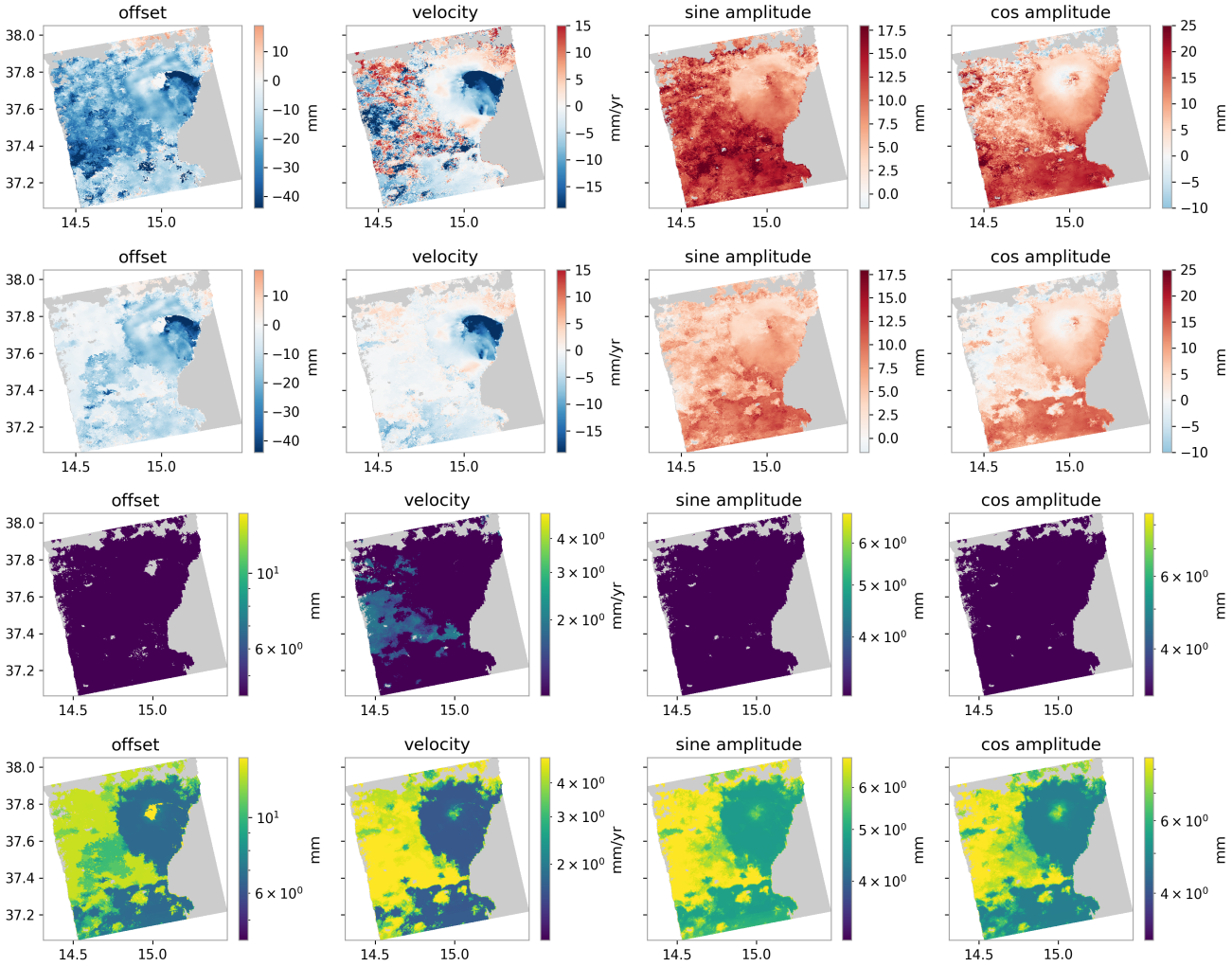

Figure S13. Same as Figure S11 for a Kalman filter for which σ_γ was changed to 1 mm or to 30 mm. Colorbars are bounded using the reference case in Figure S11 for easy comparison. Row by row from top to bottom: parameters for low σ_γ, parameters for high σ_γ, standard deviations associated with each parameter for low σ_γ and, below, for high σ_γ.

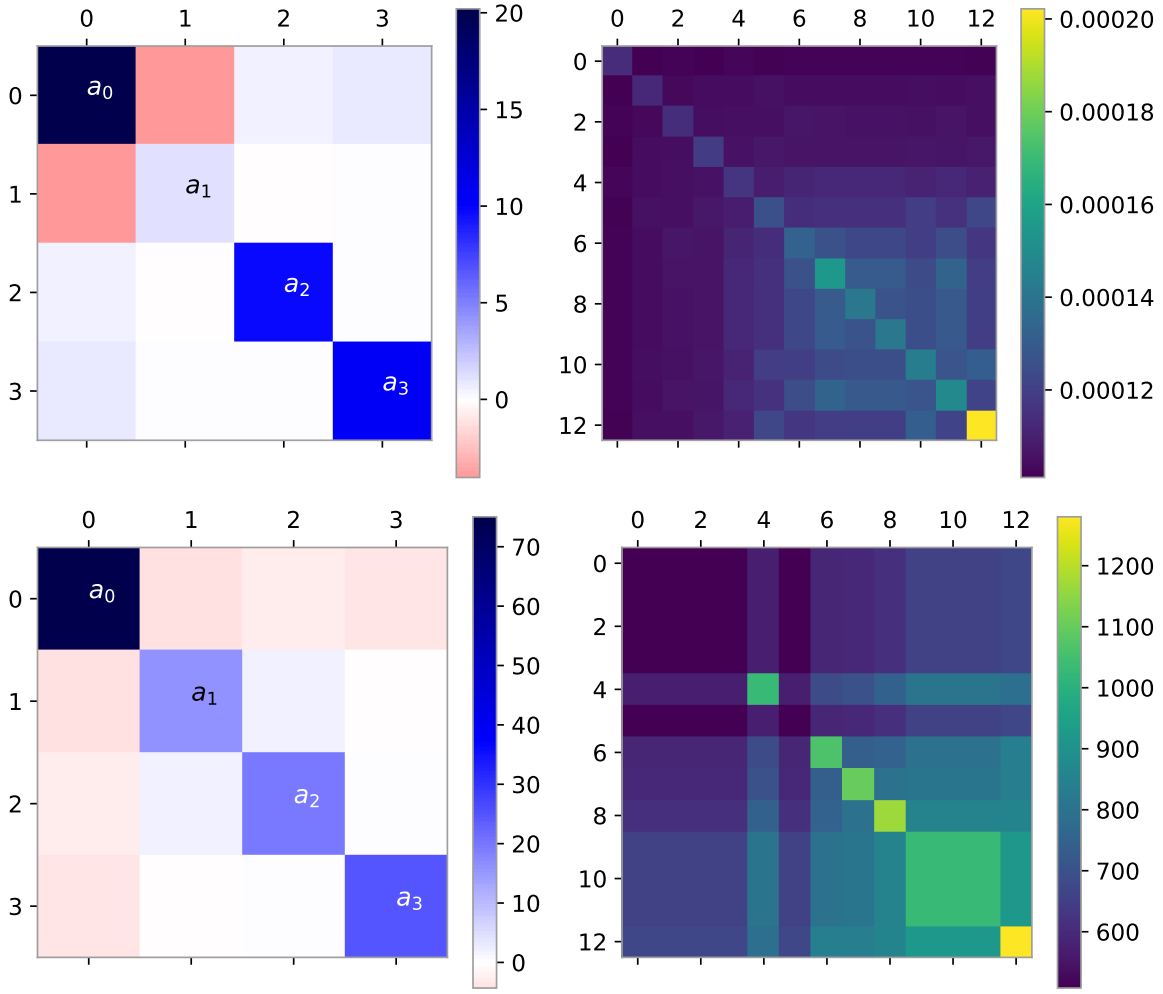

Figure S14. Same as Figure S1 for the application of the KF on Mt Etna (Section 3.2). We see the final Covariance matrix ($\mathbf{P}_{62}$) for the pixels in the KF solution at the location of GPS stations ESLN (top) and MMME (bottom).